

# Nanostructured MnO<sub>2</sub>-TiN Nanotube Arrays for Advanced Supercapacitor Electrode Material

Peng Ren

Tongji University

Chao Chen

Shaoguan University

Xiuchun Yang (✉ [yangxc3200@163.com](mailto:yangxc3200@163.com))

Tongji University

---

## Research Article

**Keywords:** Titanium nitride, nanotube arrays, nanostructured manganese dioxide, supercapacitor electrode

**Posted Date:** November 3rd, 2021

**DOI:** <https://doi.org/10.21203/rs.3.rs-1011104/v1>

**License:**  This work is licensed under a Creative Commons Attribution 4.0 International License.

[Read Full License](#)

---

**Version of Record:** A version of this preprint was published at Scientific Reports on February 8th, 2022. See the published version at <https://doi.org/10.1038/s41598-022-05167-1>.

# Abstract

Supercapacitor is an emerging and essential energy storage device to supply energy for human activities. Optimizing electrode materials is necessary for the development of high-performance supercapacitors. Herein, we synthesize different nanostructured MnO<sub>2</sub>-TiN nanotube arrays electrode materials and discuss their electrochemical performance. The synergistic effects of TiN with high conductivity and MnO<sub>2</sub> with high capacitance can extremely enhance the electrochemical performance of the electrode material. The specific capacitance of δ-MnO<sub>2</sub> nanosheets-TiN nanotube arrays can reach to 689.88 F·g<sup>-1</sup> with good magnification capacity and electron/ion transport properties. Its internal resistance and the charge transfer resistance are low as 1.183 Ω and 52.23 Ω, respectively, indicating the excellent electronic conductivity and electron diffusion. In terms of charging-discharging cycle stability, the specific capacitance retention rates are 97.2% and 82.4 % of initial capacitance after 100 and 500 cycles, respectively.

## Introduction

With the development of renewable energy, high-performance electrochemical energy storage will take into account in the future. A device with energy storage function called "Laihton bottle" was discovered by Dutch in 1746[1]. Since then, the mystery of capacitors has been gradually revealed. The research on supercapacitors(SCs) can be traced back to 1879, when Helmholtz first discovered the characteristics of electric double layer capacitance at the electrochemical interface[2]. In 1957, Becker applied for the first carbon electrode supercapacitor patent, which has a similar energy density to batteries and has a specific capacitance that is 3 to 4 orders of magnitude higher than ordinary capacitors[3]. In the researches on SCs, the electrode materials have an important effect on performance.

Generally, SCs can be divided into electrical double layer capacitors (EDLCs) and pseudocapacitors (PCs) depending on their energy storage mechanism[4], EDLCs mainly based on high surface area materials, such as carbon, graphene[5], graphite oxide[6] so on, which are all kinds of nanostructures, PCs mainly based on metal oxides and graphene-like layered metal compounds[7], using transition metal oxide (Co<sub>3</sub>O<sub>4</sub>, NiO, RuO<sub>2</sub> and MnO<sub>2</sub>, etc) nanomaterials with good electrochemical properties is a practical way to optimize the electrochemical performance of the electrode materials for the development of high-performance SCs[8].

MnO<sub>2</sub> is considered as a potential electrode material for SCs, which not only possesses electric double layer capacitance but also has high pseudocapacitance capacity as a semiconductor. The theoretical specific capacitance of MnO<sub>2</sub> can reach to 1370 F·g<sup>-1</sup> [9,10]. In 1999, Lee and Goodenough first researched on the pseudocapacitance properties of MnO<sub>2</sub> in aqueous solution and proposed that the main energy storage mechanism is the pseudocapacitance reaction in the electrode material[11]. The charge/discharge processes mainly include the adsorption/desorption of metal cations on the surface of MnO<sub>2</sub> and the intercalation/deintercalation in MnO<sub>2</sub> with rapid and reversible redox reactions[12,13]. In

addition, the crystal structure of  $\text{MnO}_2$  directly impacts on the electrochemical performance. Brousse et al. prepared  $\text{MnO}_2$  with different crystal structures and studied their electrochemical properties[14]. The results showed that the specific capacitances of one-dimensional  $\alpha\text{-MnO}_2$  and two-dimensional  $\delta\text{-MnO}_2$  are about  $110 \text{ F}\cdot\text{g}^{-1}$ , respectively. Ghodbane et al. further studied  $\text{MnO}_2$  electrode materials with different crystal structures and proposed that the specific capacitances of the  $\lambda\text{-MnO}_2$  and  $\delta\text{-MnO}_2$  with three-dimensional structures are  $241 \text{ F}\cdot\text{g}^{-1}$  and  $225 \text{ F}\cdot\text{g}^{-1}$ , respectively[15]. However, the capacitance of the SCs with simple  $\text{MnO}_2$  electrode is not high as expected due to the low conductivity of  $\text{MnO}_2$  ( $10^{-3}\sim 10^{-4} \text{ S}\cdot\text{m}^{-1}$ )[16]. Therefore,  $\text{MnO}_2$  needs to be compounded with other materials with good electrical conductivity to improve the overall electrochemical performance including specific capacitance, charge/discharge performance, and cycle characteristics. Since transition metal nitrides have great electrical conductivity, electrochemical characteristics, chemical stability and long service life, TiN, VN, CrN and TiVN are widely used as electrode materials of SCs[17-19]. TiN has been used in electric devices such as microelectronics, semiconductor device electrodes, lithium ion batteries, fuel cells and SCs as a low-cost transition metal nitride with good conductivity ( $4000\sim 55500 \text{ s}\cdot\text{cm}^{-1}$ ) and stability[20-22]. Tang et al. used urea and  $\text{TiCl}_4$  to prepare TiN as a SCs electrode material with a specific capacitance of  $407 \text{ F}\cdot\text{g}^{-1}$ [ 23].

In this work,  $\text{MnO}_2$  nanosheet spheres, nanosheets, nanorod spheres, and nanorods are synthesized on TiN nanotube arrays for obtaining a electrode material for SCs, where the nanostructured  $\text{MnO}_2$  is more chemically stable than  $\text{MoS}_2$ [24] and has better electrochemical performance than layered  $\text{MnO}_2$ [25]. The composition and morphology are measured by using XRD, SEM and EDS. The electrochemical performances of all samples in a electrolyte containing  $\text{K}^+$  are measured and discussed.

## Methods

*Preparation of  $\text{TiO}_2$  NTAs on mesh(TONM):* All reagents are analytical grade and used without further purification. A large piece of raw Ti mesh (50 meshes, 99.5% purity) with thickness of 0.12 mm was cut into square pieces of  $2.5 \times 2.5 \text{ cm}^2$ , which were ultrasonically degreased in acetone, isopropanol, and methanol for 15 min, respectively, then chemically etched in a mixture of HF and  $\text{HNO}_3$  aqueous solution (HF: $\text{HNO}_3$ : $\text{H}_2\text{O}$  = 1:4:10 in volume, total 20 mL) for 10 s, afterwards rinsed with deionized water and finally dried in air. Electrochemical anodic oxidation was performed at 60 V direct current voltages for 24 h in DEG solution containing 1.5 vol.% HF, using Ti mesh as the working electrode and Pt plate as counter electrode. The as-prepared samples were ultrasonically rinsed with deionized water and dried in air[25].

### Preparation of TiN NTAs on mesh(TNNM)

TONM samples in a quartz boat were placed in the heating center of a horizontal quartz tube vacuum furnace. Prior to heating, the system was evacuated and flushed with high pure  $\text{N}_2$  to eliminate oxygen. Afterwards, the furnace was heated in  $\text{N}_2$  to  $750^\circ\text{C}$ , and then changed to  $\text{NH}_3$  flow keeping a flow rate of

100 mL/min for 5 h while the temperature was maintained. Finally, the furnace cooled down to room temperature in N<sub>2</sub>.

### Preparation of MnO<sub>2</sub> modified TNNM

Different precursor solutions were employed for synthesizing MnO<sub>2</sub> nanostructures by hydrothermal synthesis method. A TNNM sample was placed at the bottom of the reaction solution in sealed 150 mL Teflon-lined autoclave, which was put into a muffle furnace for hydrothermal reaction. The solution compositions and reaction solutions are summarized in Table 1.

Table 1  
The precursor solution compositions and conditions of hydrothermal reaction for preparing nanostructured MnO<sub>2</sub>.

Solution	KMnO <sub>4</sub>	MnSO <sub>4</sub> ·H <sub>2</sub> O	HCl	H <sub>2</sub> O	Temperature [°C]	Time [h]	Sample
M-1	0.875 g	0.35 g	-	70 mL	140	3	TN-MO-SS
						12	TN-MO-S
						18	TN-MO-SR
M-2	1.106 g	-	0.88 mL	70 mL	150	6	TN-MO-RS
M-3	0.7875 g	-	1.75 mL	70 mL	150	12	TN-MO-R

### Characterization

The crystalline phase compositions of the samples were measured by a Rigaku D/Max 2550VB3+/PC X-ray diffractometer (XRD) equipped with graphite monochromatized Cu K $\alpha$  radiation ( $\lambda = 0.15405$  nm). Nanostructures and elemental distributions of the samples were characterized by a Schottky field emission scanning electron microscopy (FESEM, FEI Nova NanoSEM 450) equipped with energy dispersive spectroscope (EDS, EDAX).

### Electrochemical performance measurement

Electrochemical measurement was measured by CHI 660E electrochemical system using a three-electrode system where the samples as a working electrode, Pt foil as a counter electrode, and Ag/AgCl electrode as a reference electrode in 2 mol/L KCl solution. Cyclic voltammetry (CV) curves were obtained in a voltage range from -0.2 V to 0.8 V at different scan rates of 5, 10, 20, 40, 60, 80 and 100 mV·s<sup>-1</sup>, respectively. Galvanostatic charge/discharge curves were recorded in a potential window from -0.2 V to 0.8 V at a series of current densities. The electrochemical impedance spectroscopy (EIS) was conducted in the frequency from 100 kHz to 10 mHz at an open-circuit potential vibration of 5 mV[25].

## Results And Discussion

Figure 1 (a and b) suggest the composition and the nanotube structure of TNTM, indicating that it consists of Ti (JCPDS card No. 65-3362) of Ti mesh and TiN (JCPDS card No. 65-5759) of vertically aligned TiN nanotubes. As shown in the XRD patterns of TN-MO-SS, TN-MO-S, TN-MO-SR, TN-MO-RS, and TN-MO-R (Figure 1c), TN-MO-SS and TN-MO-S mainly contain  $\delta$ -MnO<sub>2</sub> crystals (JCPDS card No. 80-1098), while the MnO<sub>2</sub> in TN-MO-SR, TN-MO-RS, and TN-MO-R is  $\alpha$ -MnO<sub>2</sub> (JCPDS card No. 44-0141). In addition, TN-MO-S also contains a little  $\alpha$ -MnO<sub>2</sub>. According to the SEM images in Figure 1(d-h), the MnO<sub>2</sub> nanostructures in TN-MO-SS, TN-MO-S, TN-MO-SR, TN-MO-RS and TN-MO-R are nanosheet spheres, nanosheets, nanorods, nanorod spheres and dispersed nanorods, respectively. The EDS spectra in Figure 1(d-h) insets further demonstrate the compositions of all samples. Equation (1) and (2) depict the chemical reactions for generating MnO<sub>2</sub> in M-1 (Equation (1)), M-2 and M-3 (Equation (2)) solutions [26,27]. Figure 2 shows the crystal growth process under hydrothermal reaction condition. At first, a number of crystal nuclei rapidly form in the solution, which aggregate into nanoparticles. Afterwards, nanosheets grow through the Ostwald ripening mechanism around the nanoparticles due to the particular lamellar crystal structure of  $\delta$ -MnO<sub>2</sub> and the intercalation of K<sup>+</sup>. As the hydrothermal reaction continues, the nanosheet spheres gradually disintegrate and form the intercalated nanosheets. Meanwhile, since  $\alpha$ -MnO<sub>2</sub> is more stable than  $\delta$ -MnO<sub>2</sub> thermodynamically, the  $\delta$ -MnO<sub>2</sub> phase begins to transform into the  $\alpha$ -MnO<sub>2</sub> phase with the  $\alpha$ -MnO<sub>2</sub> nuclei generating in the  $\delta$ -MnO<sub>2</sub> nanosheets. Then, the  $\delta$ -MnO<sub>2</sub> crystal domains diffuse to the  $\alpha$ -MnO<sub>2</sub> nucleus and convert into  $\alpha$ -MnO<sub>2</sub>, while  $\alpha$ -MnO<sub>2</sub> nanorods grow through the Ostwald ripening mechanism [26,28]. In M-2 and M-3 solutions, the strong reducibility of Cl<sup>-</sup> and the presence of H<sup>+</sup> greatly accelerate the chemical reaction and phase transition speed [26].

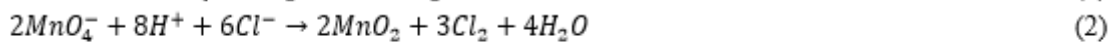


Figure 3(a and b) show the cyclic voltammetry curves with the sweep speed of 5 mV·s<sup>-1</sup> and corresponding specific capacitances of samples TN-MO-SS, TN-MO-S, TN-MO-SR, TN-MO-RS, and TN-MO-R. TN-MO-S has the largest specific capacitance of 689.88 F·g<sup>-1</sup>. The specific capacitances of TN-MO-SS, TN-MO-SR, TN-MO-RS and TN-MO-R are 577.45 F·g<sup>-1</sup>, 407.23 F·g<sup>-1</sup>, 143.65 F·g<sup>-1</sup> and 152.03 F·g<sup>-1</sup>, respectively. Figure 3(c and d) show the cyclic voltammetry curves with the sweep speed of 5 mV·s<sup>-1</sup> and corresponding specific capacitances of TNTM, TO-MO-S and TN-MO-S. Obviously, the specific capacitance of TN-MO-S is about 6.1 times and 2.5 times of TNTM and TO-MO-S, respectively. The results demonstrate that the synergistic effects of MnO<sub>2</sub> nanosheets and TiN nanotube arrays significantly increase the specific capacitance. The specific capacitance mainly depends on the surface area of MnO<sub>2</sub> and the capacity of K<sup>+</sup> [29]. TN-MO-S and TN-MO-SS have large specific surface area and great capacity for K<sup>+</sup> due to layered crystal structure (Figure 4) [11]. The 3D structures formed by the intercalation of nanosheets benefit to energy storage with electrolyte ions intercalation/deintercalation and provide numerous chemical reaction sites. In addition, the contact between MnO<sub>2</sub> nanosheets and TiN nanotubes is more sufficient and tighter than that of MnO<sub>2</sub> nanorods, which facilitates the transport

of electrons between the substrate and the active substance (Figure 3e). Since the hydrothermal reaction time during the preparation of TN-MO-S is longer than TN-MO-SS, TN-MO-S contains more hydrates to adsorb more  $K^+$  than TN-MO-SS, which further improves the pseudo-capacitance. TiN nanotube arrays can not only provide high-speed channels for electron transport, but also expands the specific surface area as a support for active substances providing more space for the ion intercalation/deintercalation during the electrochemical process. Besides, TiN nanotube arrays directly contact with the substrate without the requirement of adhesion agent, which efficiently promotes the charge transfer between the interface.

Figure 5(a and b) show the curves and corresponding specific capacitances of TN-MO-S at different scan rates. The cyclic voltammetry curves maintain symmetrical shapes from  $0.005 \text{ V}\cdot\text{s}^{-1}$  to  $0.1 \text{ V}\cdot\text{s}^{-1}$ , indicating the magnification capacity of the electrode material. The specific capacitance decreases with the increase of scan rate because of the insufficient Faraday reaction time at high scanning rate. Figure 5c shows the charging-discharging curves of TN-MO-S at different current densities. The nearly symmetrical triangular outlines manifest the capacitive and reversible characters of the electrode. The Nyquist plot, corresponding fitted curve and the equivalent circuit of TN-MO-S are shown in Figure 5d. The internal resistance ( $R_1$ ) and the charge transfer resistance ( $R_2$ ) of the electrode are low as  $1.183 \Omega$  and  $52.23 \Omega$ , respectively, indicating the excellent electronic conductivity and electron diffusion. Figure 5e depicts the cycle stability of TN-MO-S by charging-discharging measurements at a current density of  $2 \text{ A}\cdot\text{g}^{-1}$  for consecutive 500 cycles. The specific capacitance of the electrode maintains 97.2% and 82.4% of initial capacitance after 100 and 500 cycles, respectively. Figure 6 shows the composition and morphology of TN-MO-S after 500 charging-discharging measurement cycles. Generally, the composition and morphology hardly change as shown in Figure 6(a-c). Meanwhile, as shown in Figure 6(d and e), the amount of  $\text{MnO}_2$  nanosheets deposited in some areas of the sample is reduced, indicating that the lost of active substance is the main reason for the specific capacitance attenuation. However, it can be obviously observed in Figure 6(d and e) that  $\text{MnO}_2$  nanosheets firmly and uniformly grow on not only the nanotube array surface but also the walls of nanotubes. The close integration of  $\text{MnO}_2$  nanosheets and TiN nanotubes improves the transportation of electrons and ions so that TN-MO-S has great electrochemical performance as a SCs electrode.

## Conclusions

In summary, various  $\text{MnO}_2$  nanostructures are synthesized on TiN nanotube arrays by hydrothermal method including nanosheet spheres, nanosheets, nanorod spheres, and nanorods for developing an advanced electrode material of SCs. The TiN nanotubes with excellent conductivity and great specific surface area provide highly efficient paths for charge transport and more electrochemical reaction sites. The nanostructured  $\text{MnO}_2$  with high theoretical specific capacitance of  $1370 \text{ F}\cdot\text{g}^{-1}$  improves the pseudocapacitance reaction and specific capacitance of the electrode material. The specific capacitance

of  $\delta$ -MnO<sub>2</sub> nanosheets-TiN nanotube arrays can reach to 689.88 F·g<sup>-1</sup> with good magnification capacity and electron/ion transport properties. Its internal resistance and the charge transfer resistance are low as 1.183  $\Omega$  and 52.23  $\Omega$ , respectively, indicating the excellent electronic conductivity and electron diffusion. In terms of charging-discharging cycle stability, its specific capacitance retention rate are 97.2% and 82.4 % of initial capacitance after 100 and 500 cycles, respectively. Hence, the synergistic effect of TiN and MnO<sub>2</sub> can extremely enhance the electrochemical performance of the electrode material for SCs.

## Declarations

### Data availability

All data included in this study are available upon request by contact with the corresponding author.

### Acknowledgements

This study was funded by Natural Science Project of shaoguan university (No. SY2020KJ03), Introduce doctoral research projects (No.407-99000604), Their financial supports are gratefully acknowledged

### Author contributions

Peng Ren and Chao Chen contributed equally to this work. Peng Ren and Chao Chen performed experimental measurements; Peng Ren and Chao Chen performed the analysis and prepared figures, Peng Ren, Chao Chen and Xiuchun Yang wrote the main manuscript text. All authors reviewed the manuscript.

### Competing interests

The authors declare no competing interests.

### Additional information

Correspondence and requests for materials should be addressed to Xiuchun Yang

**Publisher's note** Springer Nature remains neutral with regard to jurisdictional claims in published maps and institutional affiliations.

## References

1. Conway, B. E. Similarities and differences between supercapacitors and batteries for storing electrical energy. In *Electrochemical supercapacitors* 11-31(Springer, Boston, MA., 1999).
2. Conway, B. E., & Pell, W. G. Double-layer and pseudocapacitance types of electrochemical capacitors and their applications to the development of hybrid devices. *Journal of Solid State Electrochemistry*. **7**, 637-644 (2003).

3. Lu, X., Yu, M., Wang, G., Tong, Y., & Li, Y. Flexible solid-state supercapacitors: design, fabrication and applications. *Energy & Environmental Science*. **7**, 2160-2181 (2014).
4. Long, J. W., Bélanger, D., Brousse, T., Sugimoto, W., Sassin, M. B., & Crosnier, O. Asymmetric electrochemical capacitors—Stretching the limits of aqueous electrolytes. *Mrs Bulletin*. **36**, 513-522 (2011).
5. Li, Y., & Zhao, D. Preparation of reduced graphite oxide with high volumetric capacitance in supercapacitors. *Chemical Communications*. **51**, 5598-5601 (2015).
6. Kim, T. Y., Lee, H. W., Stoller, M., Dreyer, D. R., Bielawski, C. W., Ruoff, R. S., & Suh, K. S. High-performance supercapacitors based on poly (ionic liquid)-modified graphene electrodes. *ACS nano*. **5**, 436-442 (2011).
7. Ren, Y., Ma, Z., & Bruce, P. G. Ordered mesoporous metal oxides: synthesis and applications. *Chemical Society Reviews*. **41**, 4909-4927 (2012).
8. Xie, Y., & Fang, X. Electrochemical flexible supercapacitor based on manganese dioxide-titanium nitride nanotube hybrid. *Electrochimica Acta*. **120**, 273-283 (2014).
9. Meher, S. K., & Rao, G. R. Enhanced activity of microwave synthesized hierarchical MnO<sub>2</sub> for high performance supercapacitor applications. *Journal of Power Sources*. **215**, 317-328 (2012).
10. Toupin, M., Brousse, T., & Bélanger, D. Charge storage mechanism of MnO<sub>2</sub> electrode used in aqueous electrochemical capacitor. *Chemistry of Materials*. **16**, 3184-3190 (2004).
11. Lee, H. Y., & Goodenough, J. B. Supercapacitor behavior with KCl electrolyte. *Journal of Solid State Chemistry*. **144**, 220-223 (1999).
12. Zhu, J., Shi, W., Xiao, N., Rui, X., Tan, H., Lu, X., ... & Yan, Q. Oxidation-etching preparation of MnO<sub>2</sub> tubular nanostructures for high-performance supercapacitors. *ACS applied materials & interfaces*. **4**, 2769-2774 (2012).
13. Li, H., Zhang, X., Ding, R., Qi, L., & Wang, H. Facile synthesis of mesoporous MnO<sub>2</sub> microspheres for high performance AC//MnO<sub>2</sub> aqueous hybrid supercapacitors. *Electrochimica Acta*. **108**, 497-505 (2013).
14. Brousse, T., Toupin, M., Dugas, R., Athouël, L., Crosnier, O., & Belanger, D. Crystalline MnO<sub>2</sub> as possible alternatives to amorphous compounds in electrochemical supercapacitors. *Journal of the Electrochemical Society*. **153**, A2171 (2006).
15. Ghodbane, O., Pascal, J. L., & Favier, F. Microstructural effects on charge-storage properties in MnO<sub>2</sub>-based electrochemical supercapacitors. *ACS applied materials & interfaces*. **1**, 1130-1139 (2009).
16. Zhang, Y., Deng, S., Luo, M., Pan, G., Zeng, Y., Lu, X., ... & Tu, J. Defect promoted capacity and durability of N-MnO<sub>2</sub>-x branch arrays via low-temperature NH<sub>3</sub> treatment for advanced aqueous zinc ion batteries. *Small*. **15**, 1905452 (2019).
17. Liu, Can, Zhang, Zhengjun, Chen, & Limin. Novel [111] oriented γ-Mo<sub>2</sub>N thin films deposited by magnetron sputtering as an anode for aqueous micro-supercapacitors. *Electrochimica Acta*. **245**, 237-248 (2017).

18. Das, B., Behm, M., Lindbergh, G., Reddy, M. V., & Chowdari, B. V. R. High performance metal nitrides, MN (M= Cr, Co) nanoparticles for non-aqueous hybrid supercapacitors. *Advanced Powder Technology*. **26**, 783-788 (2015).
19. Śliwak, A., Moysowicz, A., & Gryglewicz, G. Hydrothermal-assisted synthesis of an iron nitride–carbon composite as a novel electrode material for supercapacitors. *Journal of Materials Chemistry A*. **5**, 5680-5684 (2017).
20. Dong, S., Chen, X., Gu, L., Zhou, X., Xu, H., Wang, H., ... & Chen, L. Facile preparation of mesoporous titanium nitride microspheres for electrochemical energy storage. *ACS applied materials & interfaces*. **3**, 93-98 (2011).
21. Jiang, Q. W. , Li, G. R. , & Gao, X. P. Highly ordered tin nanotube arrays as counter electrodes for dye-sensitized solar cells. *Chemical Communications*. **44**, 6720-6722 (2009).
22. Kong, J. Z., Xu, P., Cao, Y. Q., Li, A. D., Wang, Q. Z., & Zhou, F. Improved corrosion protection of CrN hard coating on steel sealed with TiOxNy-TiN composite layers. *Surface and Coatings Technology*. **381**, 125108 (2020).
23. Tang, S., Cheng, Q., Zhao, J., Liang, J., Liu, C., Lan, Q., ... & Liu, J. Preparation of Titanium nitride nanomaterials for electrode and application in energy storage. *Results in physics*. **7**, 1198-1201 (2017).
24. Wang, J., Zhou, Q., Xu, L., Gao, X., & Zeng, W. Gas sensing mechanism of dissolved gases in transformer oil on Ag–MoS<sub>2</sub> monolayer: a DFT study. *Physica E: Low-dimensional Systems and Nanostructures*. **118**, 113947 (2020).
25. Chen, C., & Yang, X. MnO<sub>2</sub> modified TiN nanotube arrays on Ti mesh for flexible supercapacitors electrode. *RSC advances*. **7**, 56440-56446 (2017).
26. Truong, T. T., Liu, Y., Ren, Y., Trahey, L., & Sun, Y. Morphological and crystalline evolution of nanostructured MnO<sub>2</sub> and its application in lithium–air batteries. *ACS nano*. **6**, 8067-8077 (2012).
27. Wang, X., & Li, Y. Rational synthesis of α-MnO<sub>2</sub> single-crystal nanorods. *Chemical Communications*. **7**, 764-765 (2002).
28. Xiao, W., Wang, D., & Lou, X. W. Shape-controlled synthesis of MnO<sub>2</sub> nanostructures with enhanced electrocatalytic activity for oxygen reduction. *The Journal of Physical Chemistry C*. **114**, 1694-1700 (2010).
29. Subramanian, V., Zhu, H., Vajtai, R., Ajayan, P. M., & Wei, B. Hydrothermal synthesis and pseudocapacitance properties of MnO<sub>2</sub> nanostructures. *The Journal of Physical Chemistry B*. **109**, 20207-20214 (2005).

## Figures

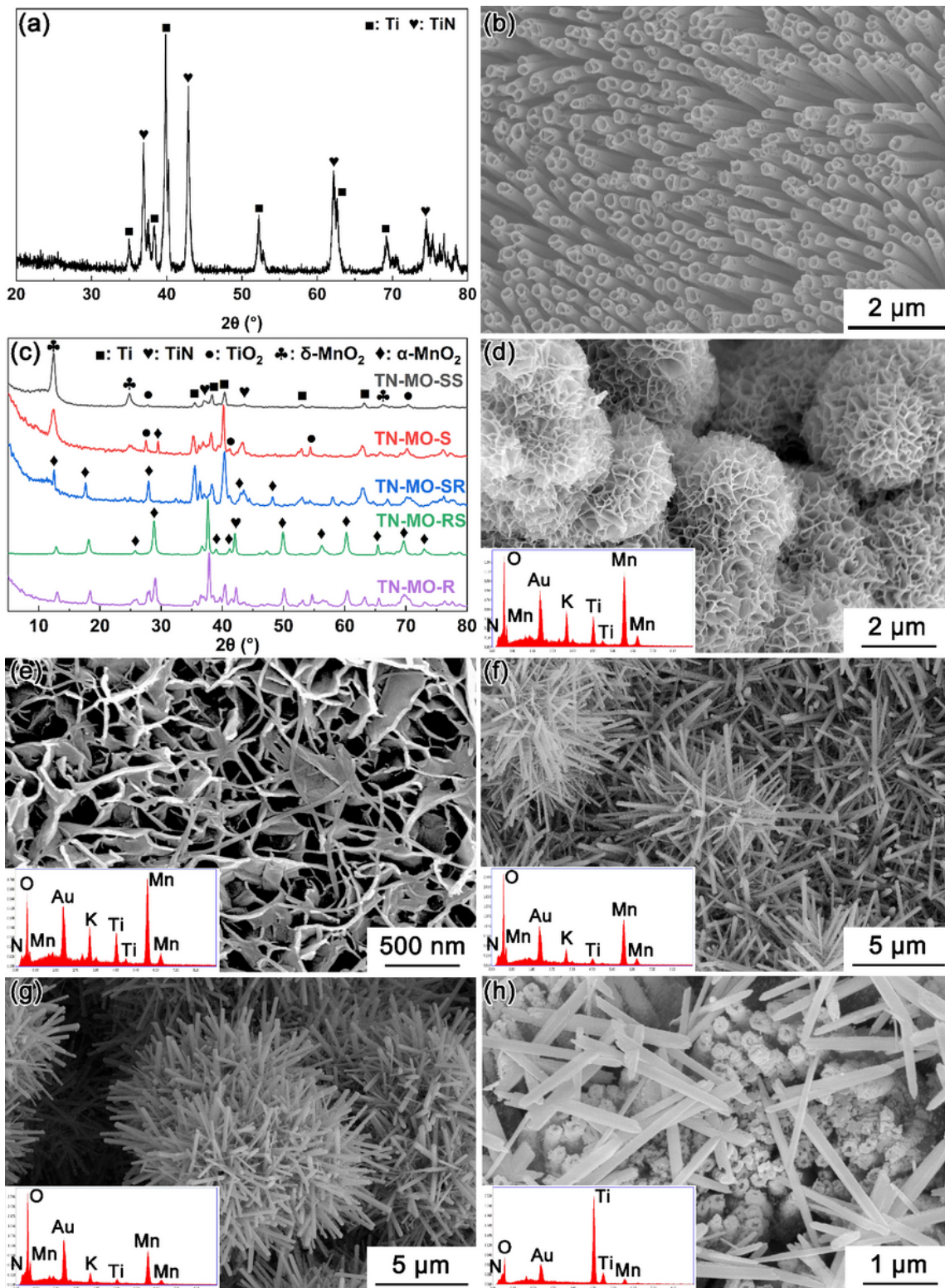


**Figure 1**

XRD pattern (a) and SEM image (b) of TNNM. XRD patterns (c) and SEM images (d-h, the insets are EDS spectra) of TN-MO-SS, TN-MO-S, TN-MO-SR, TN-MO-RS, and TN-MO-R.

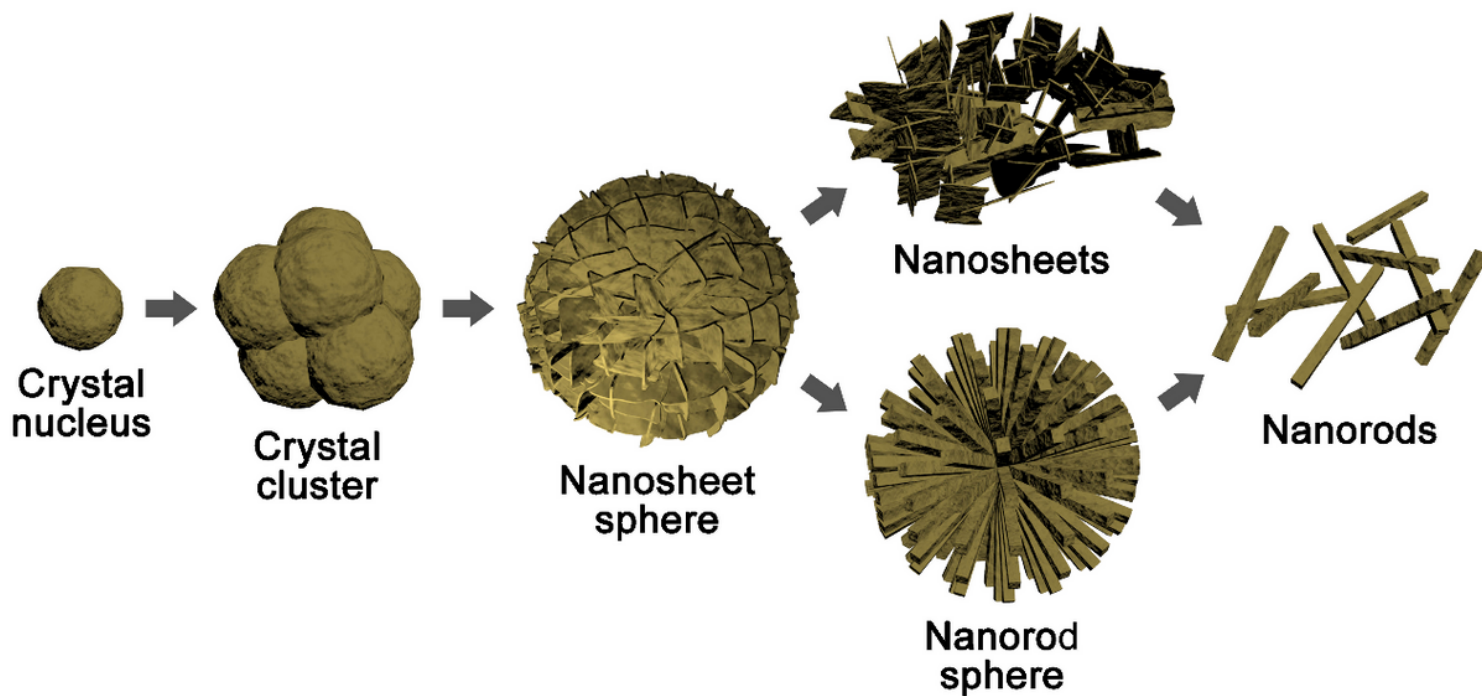
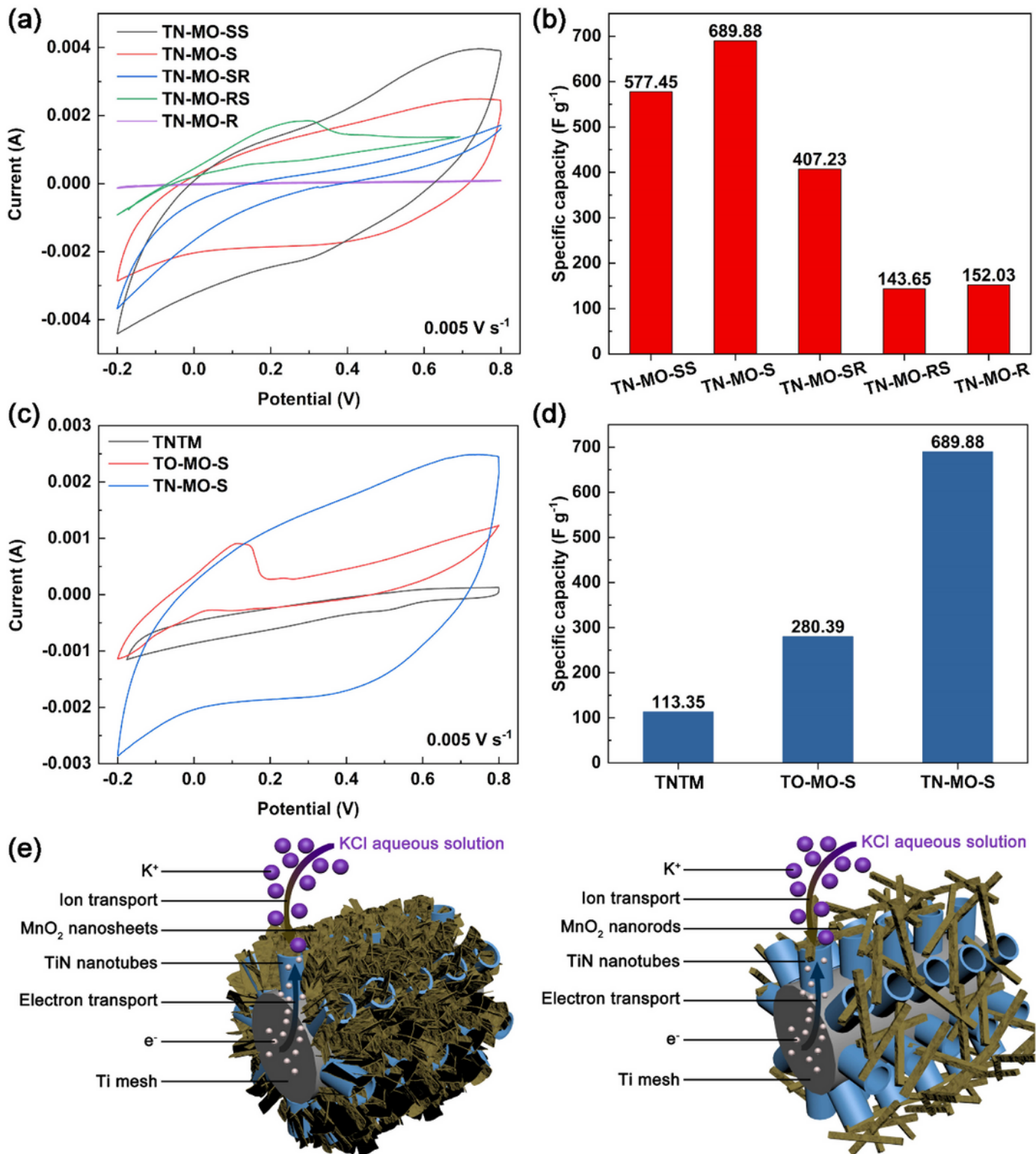


Figure 2

Schematic diagrams of MnO<sub>2</sub> nanostructure growth process.



**Figure 3**

Cyclic voltammetry curves (a) and corresponding specific capacitances (b) of TN-MO-SS, TN-MO-S, TN-MO-SR, TN-MO-RS, and TN-MO-R with the sweep speed of 5 mV·s<sup>-1</sup>. Cyclic voltammetry curves (c) and corresponding specific capacitances (d) of TNTM, TO-MO-S and TN-MO-S with the sweep speed of 5 mV·s<sup>-1</sup>. Schematic diagrams of nanostructures of TN-MO-S and TN-MO-R (e).

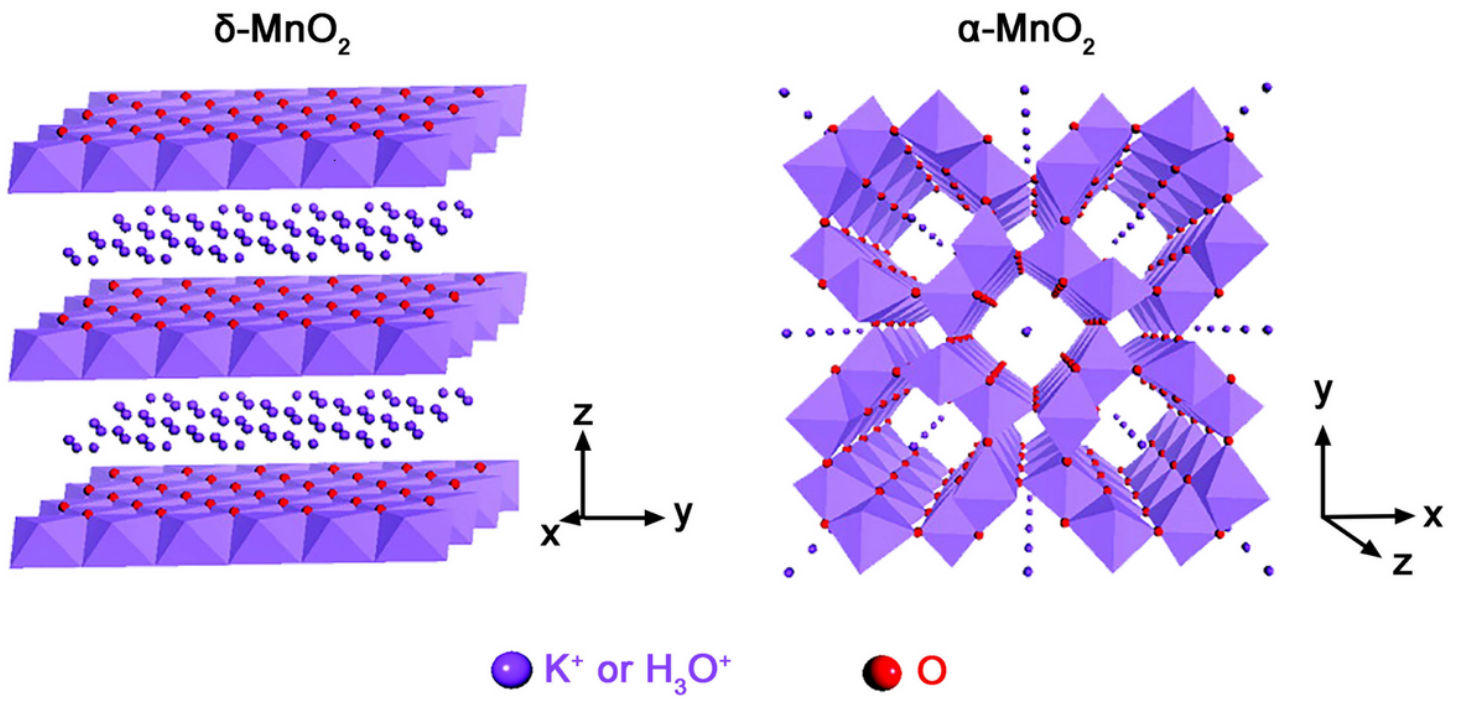
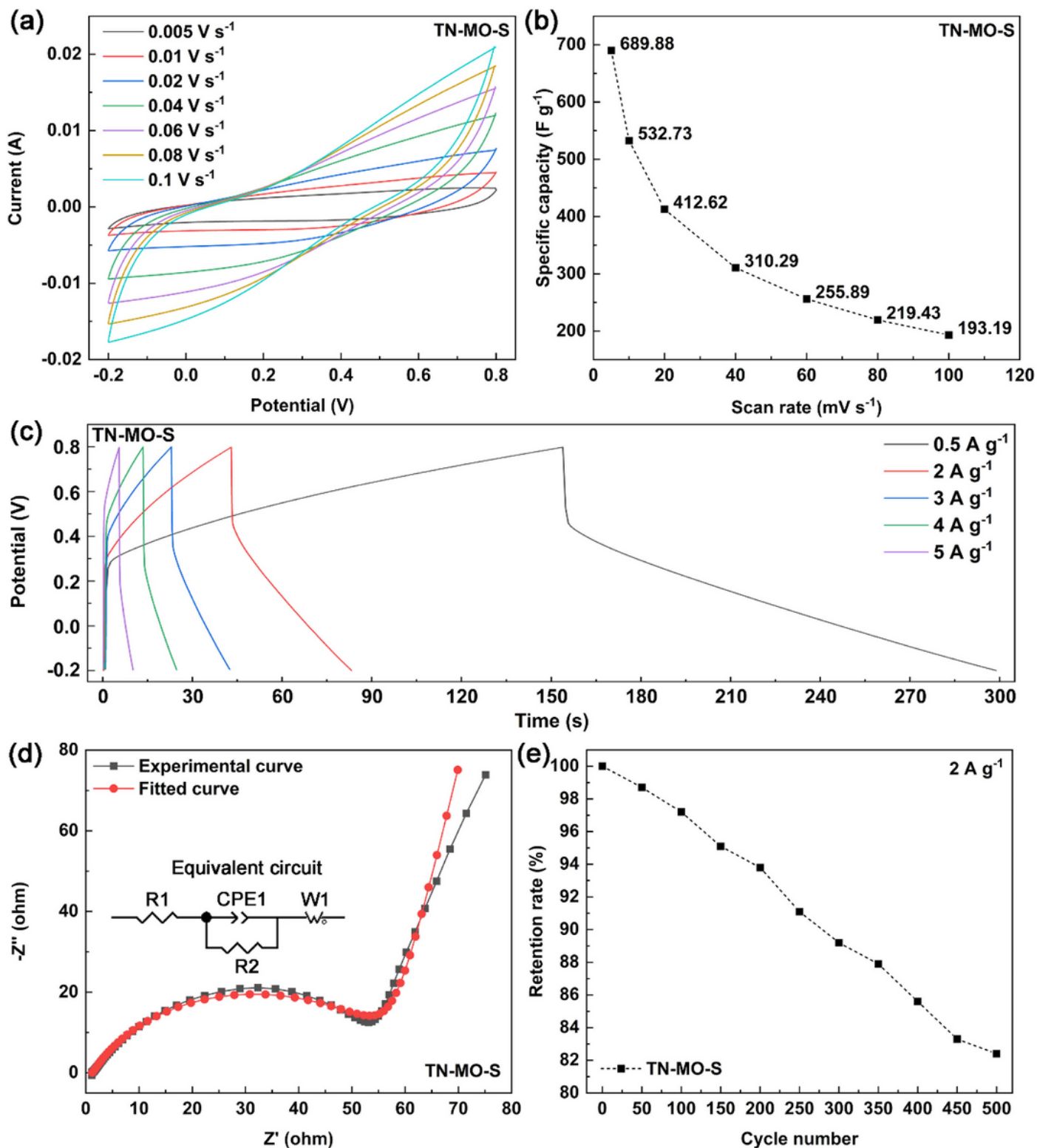


Figure 4

Schematic diagrams of  $\delta\text{-MnO}_2$  and  $\alpha\text{-MnO}_2$  crystal structure.



**Figure 5**

Cyclic voltammetry curves with different scan rates (a), corresponding specific capacitances (b), charge-discharge curves with different current densities (c), Nyquist plot and fitted curve (d, the inset shows the equivalent circuit), and the cyclic stability (e) of TN-MO-S.

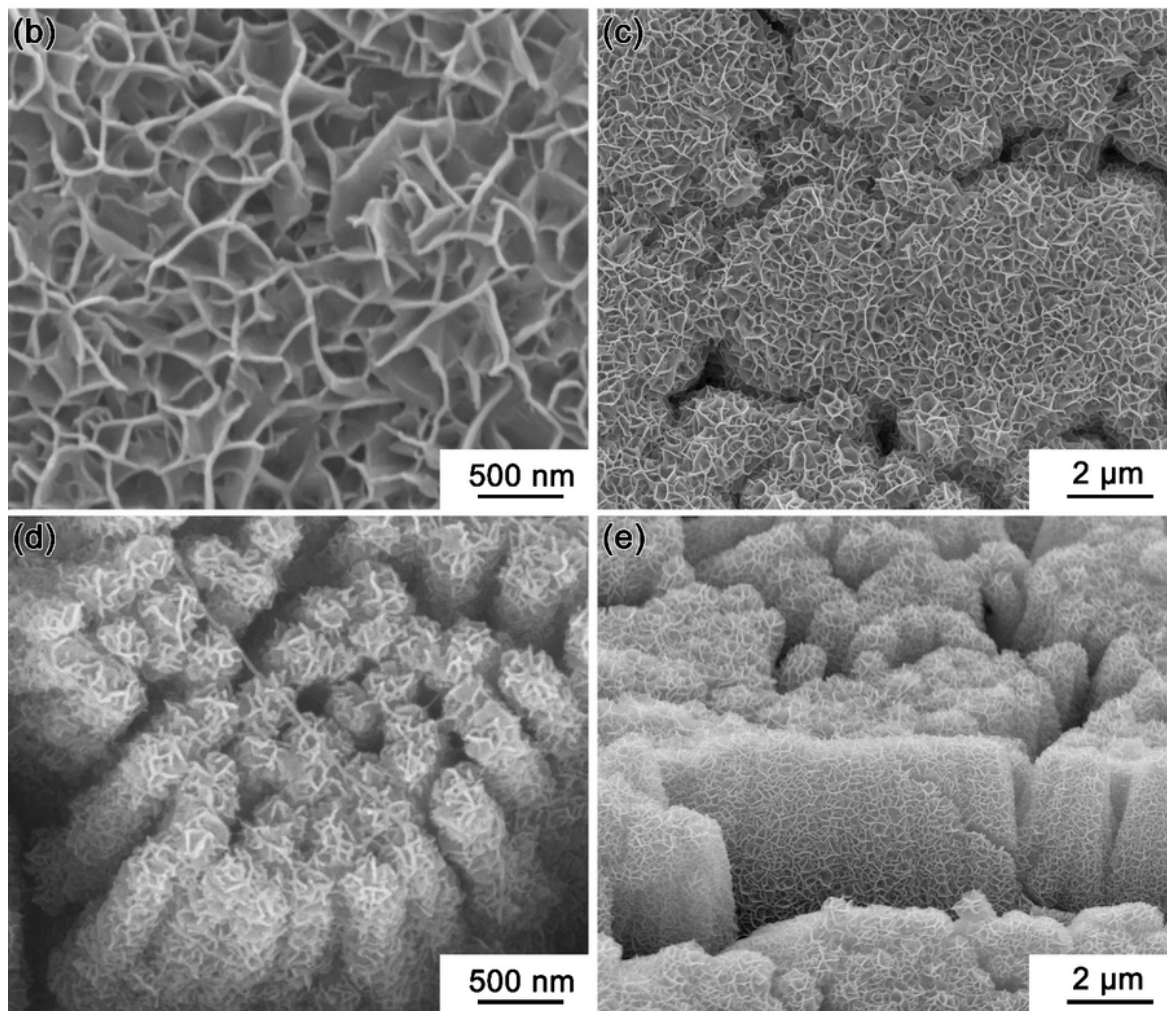
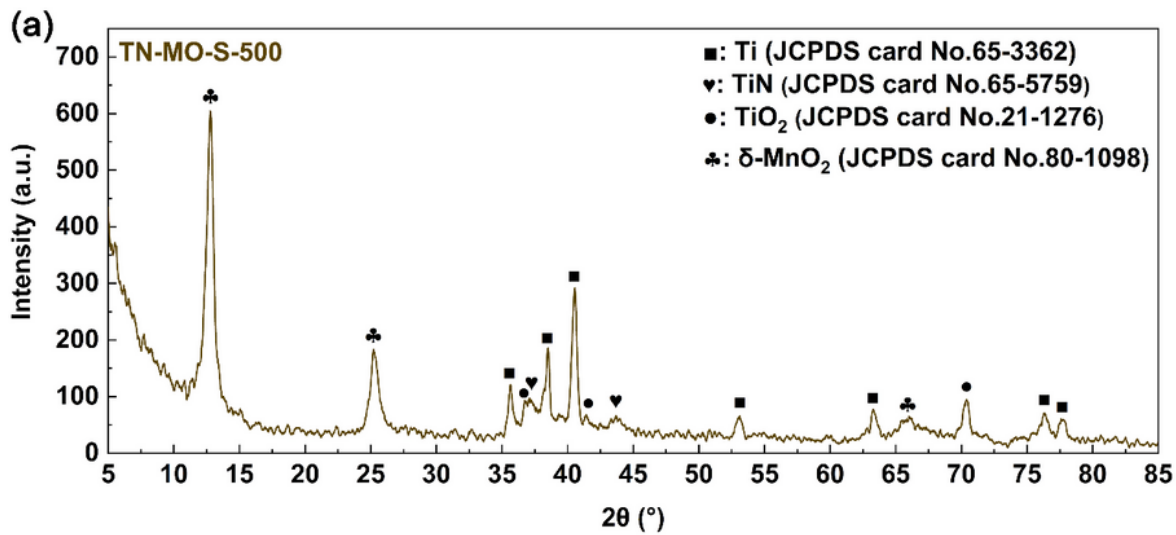


Figure 6

XRD pattern (a) and SEM images (b-e) of TN-MO-S-500.

## Supplementary Files

This is a list of supplementary files associated with this preprint. Click to download.

- [SupplementaryMaterial.docx](#)